Supplement of The Cryosphere, 19, 1937–1954, 2025
https://doi.org/10.5194/tc-19-1937-2025-supplement

The Cryosphere
Open Access

Supplement of

A facet-based numerical model to retrieve ice sheet topography from Sentinel-3 altimetry

Jérémie Aublanc et al.

Correspondence to: Jérémie Aublanc (jaublanc@groupcls.com)

Section S1: Description of the numerical facet-based model and associated computational time (section 2)

1) Numerical modelling description

Symbol	*Parameter*	*Value*
c	Speed of light	299792458 m s-1
Fc	Carrier Frequency	13.575 GHz
G_0	One way antenna gain	42 dB
θ_{3dB}	Antenna beamwidth at -3dB	1.35°
$\sigma 0$	Backscatter coefficient	6 dB
Bw	Received bandwidth	320 MHz
$Rref$	Tracker range reference	43 (index in the window analysis)
N_w	Number of samples in the window analysis	128 range gates
N_{ew}	Number of samples in the extended window analysis	512 range gates
FP_s	DEM surface extracted around nadir	35 km

Table S1: Input parameters of the numerical model. Note: the satellite and nadir positions and the altimeter tracker ranges are read in the ESA L2 Products.

The following figure shows the conceptual flow chart of the facet-based simulation module, described in section 2.2:

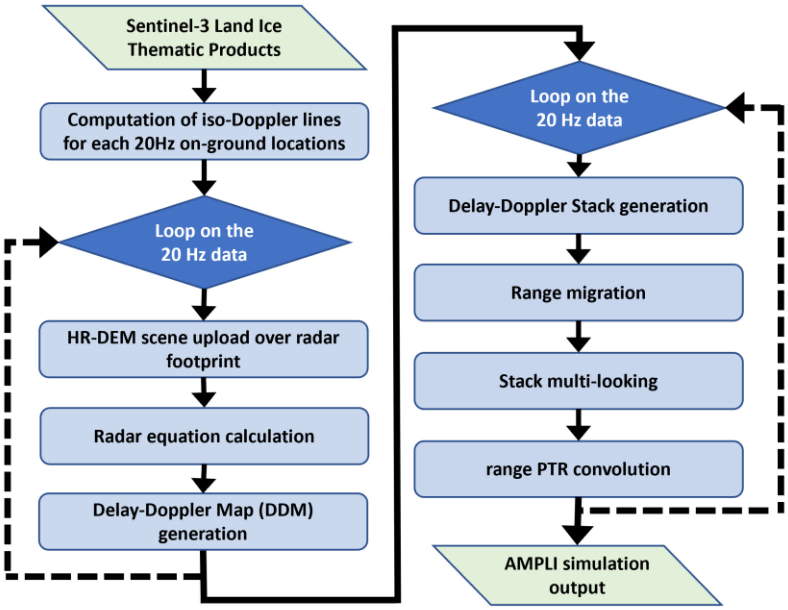

Figure S1: Flow chart of the facet-based simulation module implemented in AMPLI.

a) Pre-processing

The AMPLI software takes as input a level-2 Sentinel-3 Land Ice Thematic Products, Baseline Collection n°5. The software processes separately and independently each equator-to-equator track disseminated by ESA in the Copernicus Data Space Ecosystem (770 tracks per radar cycle of 27 days). https://dataspace.copernicus.eu/

During a pre-processing procedure, the 20 Hz records located over the Antarctic ice sheet and ice shelves are selected, using the surface mask from BedMachine dataset, version n°3 for Antarctica (Morlinghem et al., 2020).

b) Iso-Doppler lines computation

For each 20 Hz record, we determine a vector of points distributed in the cross-track direction, sampled at 10 m, and extending up to ± 15 km from nadir. These points correspond to iso-Doppler lines, that are further used to reproduce the delay-Doppler beams, as explained in step (d). They are illustrated in the main text in Fig. 1, annotated as "iso-Doppler frequencies" (plotted in cyan colour).

c) Radar equation calculation

A loop is performed on the 20 Hz measurements. For each of them, a 35 km x 35 km area of the REMA mosaic DEM (version 2.0, 10 m resolution) is read. The extracted matrix is centred around nadir location. The energy backscattered at snow-air interface P_{fs} *(x,y)* is computed for each facet of the 35 km x 35 km DEM, according to the Brown model (Brown, 1977). All equations are adapted to account for a spherical Earth. The geometrical computations are performed in the Antarctic Polar Stereographic projection (EPSG:3031).

$$P_{fs}\,(x,y) = \frac{\lambda\,\sigma_0}{(4\pi)^3} \int_A \left(\frac{G^2(\theta)}{r^4}\right) dA \qquad \text{(S1)}$$

where:

- **λ is the radar wavelength = $\frac{c}{Fc}$**

- ***r* is the distance between antenna and the facet**

$$r\,(x,y) = \sqrt{dx^2 + dy^2 + dz^2} \qquad \text{(S2)}$$

dx **and** ***dy*** *are the horizontal distances between nadir and the DEM facet, calculated with the cartesian stereographic coordinates.*

dz *is the vertical distance between the satellite altitude and the facet height.*

- ***G*(θ) the antenna pattern modelled with a Gaussian function:**

$$\mathrm{G}\,(\theta) = G_0\, e^{-\frac{2}{\gamma}\sin^2\theta} \qquad \text{with } \gamma = \frac{2\,\sin^2\frac{\theta_{3dB}}{2}}{\ln(2)} \qquad \text{(S3)}$$

ϑ *being the angle from the antenna boresight axis to the line from the sensor to dA.* ϑ_{3db} *is the antenna beamwidth at -3 dB.*

- **σ_0 is the backscattering coefficient, per unit scattering area**

$\boldsymbol{\sigma_0}$ is taken as a constant (= 6 dB). We neglect the $\boldsymbol{\sigma_0}$ variation with angle of incidence, by making the assumption that the impact remains relatively minor compared to the antenna aperture. We assume this assumption can be taken, based on the relative homogeneity of the ice sheet surface (at the footprint scale), in terms of backscattering properties. Brown (1977) also took this assumption for the ocean surface. This simplification was confirmed to be valid, given the relatively good agreement obtained in the simulated waveforms, when they were compared to Sentinel-3 ones (as presented section 2.4, and in supplementary material S2). Nevertheless, it would be still worthwhile considering the σ0 variation with angle of incidence, for further refining the physical modelling.

The "6 dB" value was chosen for all simulated waveforms, wherever the location of the satellite, as this is approximatively the average value found over Antarctica with the equation indicated in supplementary S3. However, since the simulated waveform is finally normalised by its maximum value during the processing, the absolute value of the $\boldsymbol{\sigma_0}$ has no impact on the topography retrieved after relocation and retracking.

- A **is the area of a surface facet** (constant set to 1 for the sake of simplicity)

In addition, a range index R_i is attributed to the facets, given the satellite-facet distance and the on-board tracker command, according to:

$$R_i\ (x, y)\ = \left(\frac{r - Tr}{\alpha}\right) + R_{ref} \qquad \text{(S4)}$$

Where:

$\boldsymbol{\alpha}$ is the altimeter vertical resolution = $\dfrac{c}{2\ Bw}$

$\boldsymbol{T_r}$ the altimeter tracker range, variable "*tracker_range_20_ku*" in the ESA L2 product. In order to use the initial tracker range of the altimeter, the offset applied in the PDGS during the delay-Doppler processing with extended window is removed (variable "*range_shift_waveform_20_ku*" in the ESA L2 product).

$\boldsymbol{R_{ref}}$ the reference index of the tracker range in the window analysis.

d) Delay-Doppler map generation

As mentioned in the main text, DDMs are constructed by integrating the energy $P_{fs}\ (x, y)$, given the facet-satellite distance in slant range (range-time domain, t), and in along-track (Doppler frequency domain, f).

In the ESA PDGS, the on-ground spacing of the "*lat_20_ku*" and "*lon_20_ku*" coordinates are determined based on the delay-Doppler along-track resolution. Thus, two consecutive 20 Hz measurements are separated by ~330 m on-ground (slightly varying along the track with satellite altitude and velocity). We take advantage of this configuration to simulate the Delay-Doppler Maps (DDM) at every 20 Hz record. For each of the 20 Hz points, the 31 previous and 32 next "*lat_20_ku*" and "*lon_20_ku*" coordinates are selected and considered as central positions of the 64 delay-Doppler beams (the case of data gap within a track is handled). The 64 delay-Doppler beams constituting the DDM are computed by integrating the backscattered energy P_{fs} along the 64 corresponding iso-Doppler lines, determined in (b), and sorted in range gate according to R_i value.

Following ESA PDGS approach, we calculate first the DDMs along the track. The delay-Doppler stacks are generated in a second step, described in (e). In addition, for each of the 64 delay-Doppler beams of the DDM (f, t), a histogram of the energy backscattered is constructed, as a function of:

- the slant-range distance between the facet and the satellite (t)
- the cross-track distance between the facet and the ground track (u)

This signal is called the Cross-Track Backscatter Distribution: CTBD (f, t, u), and is further used in the relocation processing.

Note: In this facet-based modelling, the DDMs are directly simulated in amplitude (I^2+Q^2), at 20 Hz rate. Therefore, there is no need to perform the beam-forming (i.e. along track FFT) and beam-steering operations, that are part of the UF-SAR processing as applied to a burst of real complex pulses.

e) Delay-Doppler stack generation

A second loop is performed on the 20 Hz records. The delay-Doppler stacks are generated following the PDGS architecture:

- The delay-Doppler stack is constructed by gathering the delay-Doppler beams from different DDM. These beams sample the same delay-Doppler footprint on-ground, therefore from different look angles along the satellite track. As mentioned in the main text, the simulated stacks include 45 single looks (available at 20 Hz rate) to be consistent with the PDGS (180 single looks collected, generated at 80 Hz rate).
- Before range migrations, the window analysis is extended from 128 to 512 samples
- Range migrations are applied to align the single looks together in the extended window analysis. The migrations include the slant range ones, as mathematically formulated by Raney (1998). They also include the re-alignment of the tracker range commands (the central look of the stack is taken as reference).
- The multi-looking operation is performed on this extended stack, by averaging the 45 single looks in the azimuth direction. Thus, a first UF-SAR mode waveform is obtained in an extended window analysis.
- The window analysis is finally tailored, to restore the nominal 128 sample size. For that purpose, we use the variable "*range_shift_waveform_20_ku*", available in the ESA L2 product, to select the 128 samples. Therefore, this shift is the same one as applied on-ground to truncate the window analysis (in the ESA PDGS this shift is set to position the waveform main energy peak at sample n°44).

f) Pulse Target Response Convolution

The multi-looked UF-SAR waveforms are oversampled in the range-time domain to be convolved with the radar system Pulse Target Response (PTR_T), with:

$$PTR_T = \left| \frac{\sin \pi \frac{t}{T}}{\pi \frac{t}{T}} \right|^2 \qquad \text{(S5)}$$

where T = 1/Bw

After convolution, the UF-SAR waveforms are undersampled to the nominal 128 sample size. It must be noted that, after few unsuccessful tests, it was decided to not apply the Azimuth Impulse Response (AIR) to the DDM. This will be reconsidered in a future processing version.

2) Discussion related to Brown model (1977) validity over the ice sheet surface

We discuss below the five assumptions that Brown (1977) stated in the introduction of his paper. These assumptions must be met to ensure the model validity, as extracted from his paper: "*For land scatter, the situation is somewhat different, and some of the above assumptions may be violated*".

Before discussing the five assumptions, it is worth highlighting that a validation of the developed modelling has been performed over the whole Antarctic ice sheet (available in supplementary material, section S2). At this stage it remains a global validation and finer assessments, at regional scales, will have to be done in future studies. Moreover, this is not the first time that the Brown model is a starting point for the radar signal modelling over ice sheets. Different studies are available in the literature. Among the references cited in this paper: Lacroix et al. (2008), Larue et al. (2021), Helm et al. (2024).

"1 - The scattering surface may be considered to comprise a sufficiently large number of random independent scattering element"

=> Over ice sheets the radar wave reflection is considered "diffuse". Therefore, as for ocean, it is possible to take the assumption that the altimetry waveform is built with a large number of independent scatterers (as sampled within the radar footprint).

"2 - The surface height statistics are assumed to be constant over the total area illuminated by the radar during construction of the mean return"

=> This assumption is violated over ice sheets because the surface is not flat. Thus, Brown's analytical formulation cannot be directly used to accurately reproduce waveforms acquired over ice sheets (except specific cases, like over the lake Vostok area).

Thus, the advantage of a facet-based modelling is to account for the effect of terrain variation in the radar waveform shape, using an external DEM (down to metre scale roughness with REMA). As mentioned in this paper: "*In this work, we use the same FSIR formulation [as Brown] and discretized it at the DEM grid points. Hence, through this so-called "facet-based simulation", the effect of terrain roughness is integrated in the radar signal modelling, down to decametre scale variations*".

"3 - The scattering is a scalar process with no polarization effects and is frequency independent."

=> To our understanding, the antenna polarisation does not act on the radar waveform shape over ocean. However, polarisation effects have been reported for LRM altimetry over ice sheets in Remy et al. (2006) and Armitage et al. (2014). To the best of our knowledge, such effect is not yet investigated in SAR altimetry. Nonetheless, it is anticipated that the impact would be relatively minor in the waveform leading edge shape in SAR mode, because it is mainly generated with energy backscattered from surface, and not sub-surface (Aublanc et al., 2018).

"4 - The variation of the scattering process with angle of incidence (relative to the normal to the mean surface) is only dependent upon the backscattering cross section per unit scattering area, go, and the antenna pattern."

=> The assumption remains overall valid over the Antarctica and Greenland ice sheets, considering the relative surface homogeneity at the footprint scale, in terms of backscattering properties. Nevertheless, this assumption is likely violated in case of ice sheet melting (i.e. meltwater on the surface of the ice sheet), as it can occur in the Greenland ice sheet margins. Specific analyses should be planned in the future on this subject.

"5 - The total Doppler frequency spread (4 V_r/λ due to a radial velocity V, between the radar and any scattering element on the illuminated surface is small relative to the frequency spread of the envelope of the transmitted pulse (2/T, where Tis the width of the transmitted pulse)."

=> The nature of the surface has no impact on this assumption.

References

Armitage, T. W. K., Wingham, D. J., and Ridout, A. L.: Meteorological Origin of the Static Crossover Pattern Present in Low-Resolution-Mode CryoSat-2 Data Over Central Antarctica, IEEE Geoscience and Remote Sensing Letters, 11, 1295–1299, https://doi.org/10.1109/LGRS.2013.2292821, 2014.

Aublanc, J., Moreau, T., Thibaut, P., Boy, F., Rémy, F., and Picot, N.: Evaluation of SAR altimetry over the Antarctic ice sheet from CryoSat-2 acquisitions, Advances in Space Research, 62, 1307–1323, https://doi.org/10.1016/j.asr.2018.06.043, 2018.

Remy, F., Legresy, B., and Benveniste, J.: On the Azimuthally Anisotropy Effects of Polarization for Altimetric Measurements, IEEE Transactions on Geoscience and Remote Sensing, 44, 3289–3296, https://doi.org/10.1109/TGRS.2006.878444, 2006.

3) Computational time benchmark

The Central Processing Unit (CPU) time was evaluated on one of the CPU nodes available in the high-performance cluster of the Centre National d'Etudes Spatiales (CNES), in Toulouse (France). We used a single core of the node, with a processor clocked at ~3 GHz.

This benchmark has been performed with a Sentinel-3A track portion located in the East Antarctic Ice Sheet interior. The CPU time is not supposed to be significantly sensitive to the area sampled by the satellite. The CPU time is evaluated in the processing steps including "radar equation calculation" and "Delay-Doppler Map generation", steps (c) and (d) as listed above. In fact, these two processing steps are by far the most demanding ones in terms of computational time.

The computational time is evaluated with the AMPLI software version used to produce the results presented in this paper. As described section 2.1, with this version the facet-based simulation is performed by means of the 10 m resolution REMA DEM. The CPU time was also evaluated with REMA sub-sampled at 20 m and 40 m, as they could represent relevant alternatives to reduce the computational time, but at the expense of the modelling accuracy. It was nonetheless out of the scope of this study making a further sensitivity analysis of the AMPLI software performance, related to the spatial resolution of the input DEM.

The benchmark was performed using 10 seconds of Sentinel-3 acquisitions, which represents a segment length of about 66 km on-ground.

- 10 m REMA (version used in this study): ~**480** seconds of data processing (CPU time) *=> real time factor of ~48*
- 20 m REMA: ~**70** seconds (CPU time) *=> real time factor of ~7*
- 40 m REMA: ~**25** seconds (CPU time) *=> real time factor of ~2.5*

Section S2: Quantitative assessment of the AMPLI simulated waveforms (section 2.4)

In this assessment, we compare the first peak position in the window analysis between Sentinel-3 UF-SAR waveforms generated by the ESA PDGS, and the ones simulated by AMPLI. The first peak position (i.e. epoch parameter) is estimated with the OCOG/ICE-1 retracker, 50 % threshold. The analysis is performed on the data set presented section 3.1, including Sentinel-3A and Sentinel-3B measurements acquired from 9 May to 25 August, 2019.

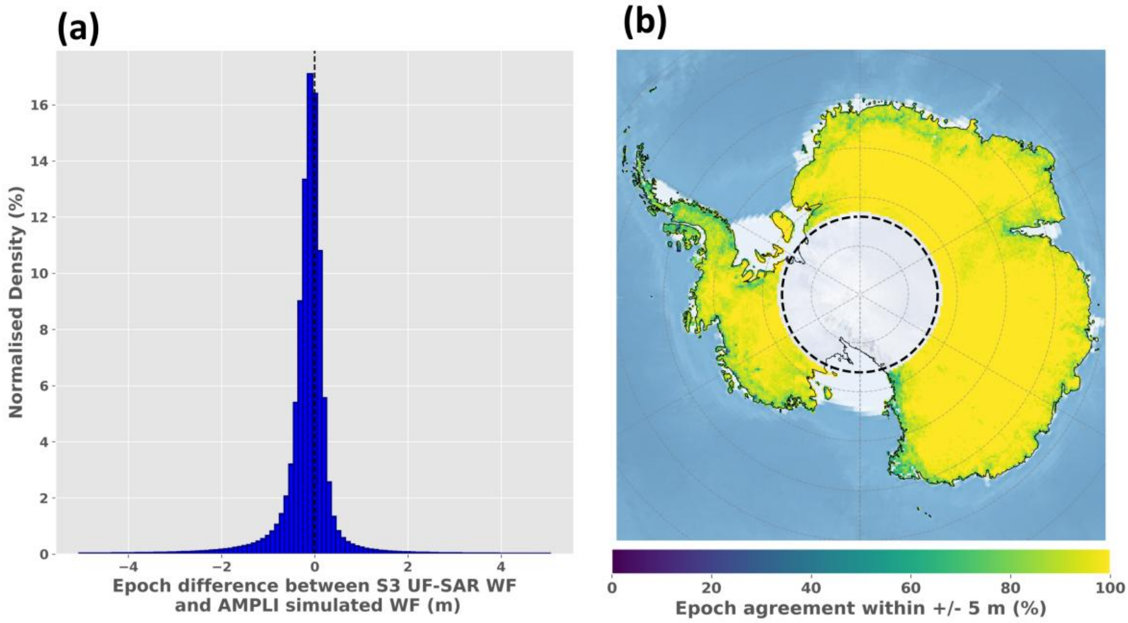

Figure S2: (a) Histogram of the difference in the epoch parameter estimated on the Sentinel-3 UF-SAR measured and simulated waveforms (b) Gridded ratio of measurements from which the epoch parameter estimated on the Sentinel-3 UF-SAR measured and simulated waveforms is within a ± 5 m agreement. Grid resolution is 25 km. 100 measurements minimum per grid points are required for the computation.

Section S3: Additional statistics in the Sentinel-3 and ICESat-2 comparisons (section 3.1)

The following numbers are the total amount of Sentinel-3A and Sentinel-3B measurements analysed in the analysis presented section 3. They were acquired by the satellites from 9 May to 25 August, 2019.

Total amount of Sentinel-3 data:	27 563 782 measurements
After common quality controls:	26 026 408 measurements (94.42%)
After second selection (AMPLI):	25 037 763 measurements (90.84%)
After second selection (ESA L2):	25 429 092 measurements (92.26%)

Note: *The percentage under bracket indicates the ratio of measurements relative to the total amount of Sentinel-3 20 Hz measurements*

Quality controls, common selection

Quality controls	WF peak detection	SNR	DEM coverage	SUM
Data discarded (%)	4.67%	1.83%	0.73%	**5.58%**

Table S2: Common quality checks applied to the Sentinel-3 elevations over the Antarctic ice sheet data set. The percentages are relative to the total amount of measurements. In the second table the percentages are relative to the amount of measurements after first selection.

Quality controls, second selection specific to each data set

	Quality controls	deviation to DEM > 50m	Retracking or Relocation failures	Surface ambiguities	Agreement data vs simulation	AMPLI relocation failures	**SUM**
ESA L2	**Data discarded (%)**	**2.14 %**	**0.03%**	***Not applicable***	***Not applicable***	***Not applicable***	**2.17%**
AMPLI	**Data discarded (%)**	**< 0.001%**	***Not applicable***	**2.34%**	**0.52%**	**0.88%**	**3.59%**

Table S3: Quality checks applied to the Sentinel-3 elevations over the Antarctic ice sheet data set. The percentages are relative to the amount of measurements after first selection.

Brief description of quality controls:

- **WF peak detection:** the measurement is discarded if no clear energy peak in the UF-SAR waveform is identified. The peak detection is based on the Leading Edge Detection (LED) algorithm described in Aublanc et al. (2021). For AMPLI, the peak detection is anyway mandatory to estimate the altimeter range, as described in section 2.3. We decided to apply this critera to ESA L2 measurements, for the sake of fair comparison between both data set.
- **Signal to Noise Ratio (SNR):** A backscatter coefficient (Sigma-0) is computed for all measurements (dB unit), according to:

$$Sigma0 = 10 * log_{10}(A_{max}) + S_f + S_b + C_o \qquad \text{(S6)}$$

where A_{max} is the maximum amplitude of the Sentinel-3 UF-SAR waveform,
S_f is a scaling factor, read in the Land Ice Thematic Product (variable "*scale_factor_20_ku*"),
S_b is a systematic bias, applied in the ESA Processor, equal to -0.65 dB,
C_o a calibration offset, calculated to roughly align this Sigma-0 with the one from the SAMOSA physical retracker (calibration performed over the ocean), equal to -18 dB

The measurement is discarded if the Sigma-0 is lower than -12 dB. In fact, below this threshold we noticed that approximately less than 50% of the waveforms have a clear energy peak (based on the LED algorithm). Therefore, we considered that the measurement is not reliable. This criterion is already used within the Sentinel-3 Mission Performance Cluster (MPC) project, to check the measurement quality over the polar ice sheets.

- **DEM coverage:** the measurement is discarded if the DEM is not 100% complete in the cross-track direction to the nadir point, up to ± 8 km (i.e. REMA value found at "*-9999*")
- **Deviation to DEM:** the measurement is discarded if the altimetry elevation deviates by more than 50 meters to the REMA value, 10 m version (the DEM value is bi-linearly interpolated at the point of first radar return coordinates).
- **Retracking or Relocation failures** (applicable only to ESA L2 elevations). After the first common quality controls, ~0.03% of the remaining range estimations do not have a physical value (in the parameter "*range_ocog_20_ku*"). This is most likely due to failures in the retracking or relocation algorithms.
- **Surface ambiguities** (applicable only to AMPLI elevations only). Ambiguity in the estimated point of first radar return, as described section 2.3. Either because distinct facet clusters contribute to the identified energy peak, with no one found predominant, or because the facet cluster illuminates a surface larger than 6 km in the cross-track direction.
- **Agreement data vs simulation** (applicable to AMPLI elevations only). Two quality controls are performed to check the simulation validity. (1) Firstly, we check the absolute cross-correlation delay between Sentinel-3 UF-SAR waveform and AMPLI simulated waveform remains below 30 range gates (~ 14 m) (2) Secondly, after cross-correlation, we check a waveform leading edge is detected in the AMPLI UF-SAR simulated waveform using the LED algorithm. The position of this waveform leading edge must be relatively close to the one detected in the Sentinel-3 UF-SAR mode waveform (maximum delay allowed is 12 range gates ~ 5.6 m).
- **AMPLI relocation failures** (applicable to AMPLI elevations only). They correspond to measurements for which no energy is found in the CrossTrack Backscattered Distribution (CTBD) signal. These errors are detected for ~0.88% of the measurements (after first common quality controls) and will be investigated in the future.

Section S4: Data sampling over Pine Island drainage basin (section 3.1)

Illustration of the data sampling achieved over Pine Island drainage basin, with AMPLI processing applied to Sentinel-3A (green) and Sentinel-3B (blue) measurements, after data editing presented section S3. One orbit cycle of both satellites is displayed, n°47 and n°27 respectively for Sentinel-3A and Sentinel-3B (corresponding to measurements acquired during the Antarctic winter 2019). The topography is estimated at the point of first radar return, which explains the non-linear paths on-ground.

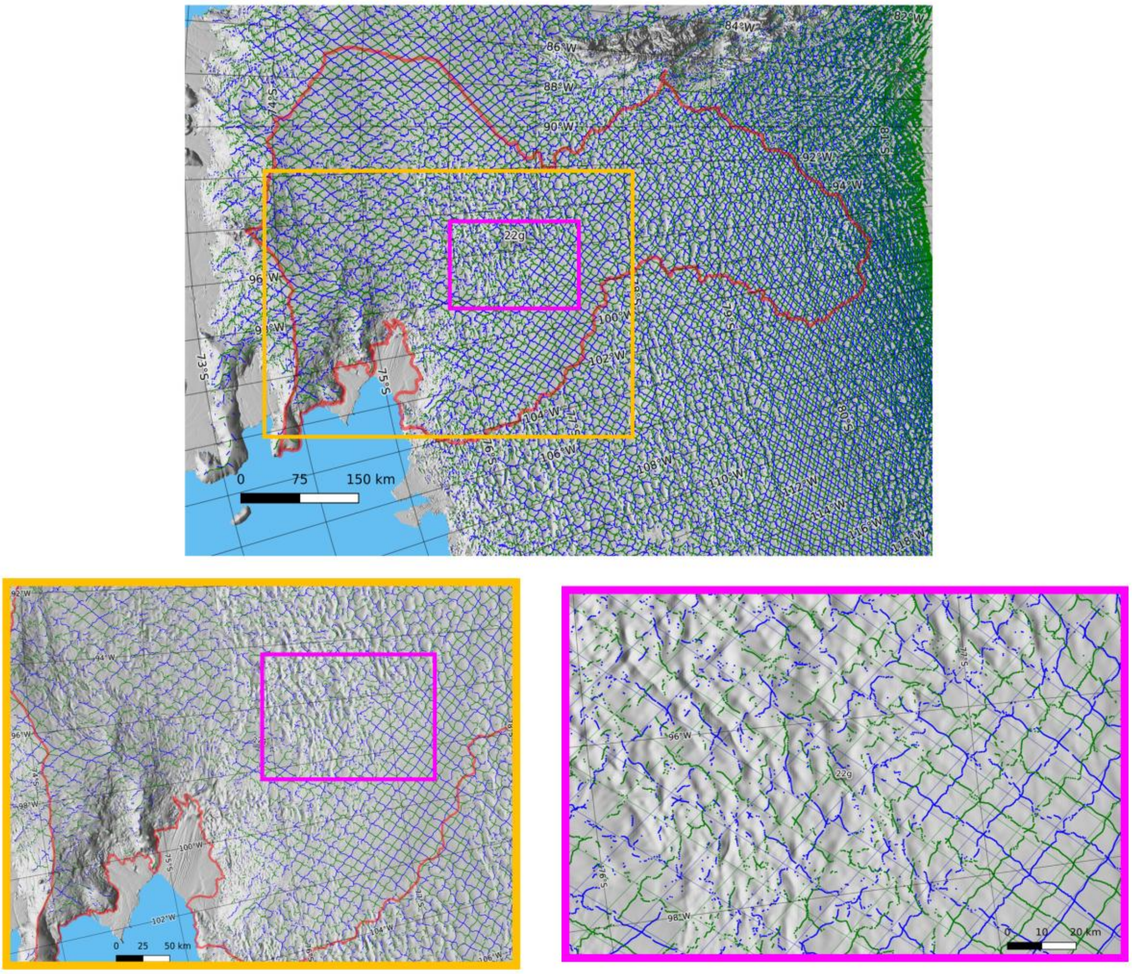

Figure S3: Data sampling over Pine Island drainage basin (red outline) with AMPLI processing applied to one orbit cycle of Sentinel-3A (green) and Sentinel-3B (blue) measurements. Yellow and magenta boxes are zoom views of the top figure.

Section S5: Alternative Sentinel-3 SEC computation (section 4.2)

To confirm the validity of the Sentinel-3 Surface Elevation Change (SEC) presented in this study (section 4.4), the SEC was calculated with an alternative method. It is based on differences between Sentinel-3 and ICESat-2 ATL06 nearly co-located measurements in space and separated by 3 years in time. The method comprises the main operations:

1) Computation of surface elevation difference between Sentinel-3 and ICESat-2 ATL06 measurements separated by 3 years (+/- 46 days). With Sentinel-3 measurements acquired from 9 May to 25 August, 2019.
2) The elevation differences are gridded in a polar stereographic projection, 20 km resolution, same grid coordinates as ICESat-2 ATL15 products. 30 nearly co-located measurements were required for the computation. This provided an initial estimate of the gridded SEC.
3) In order to remove the initial bias between the two missions, the same computations and same grids are calculated with Sentinel-3 and ICESat-2 ATL06 nearly co-located measurements (in space **and time**), acquired in 2019.
4) The final gridded SEC is obtained by subtracting the "calibration grid", to the initial SEC grid (step 2 grid – step 3 grid).

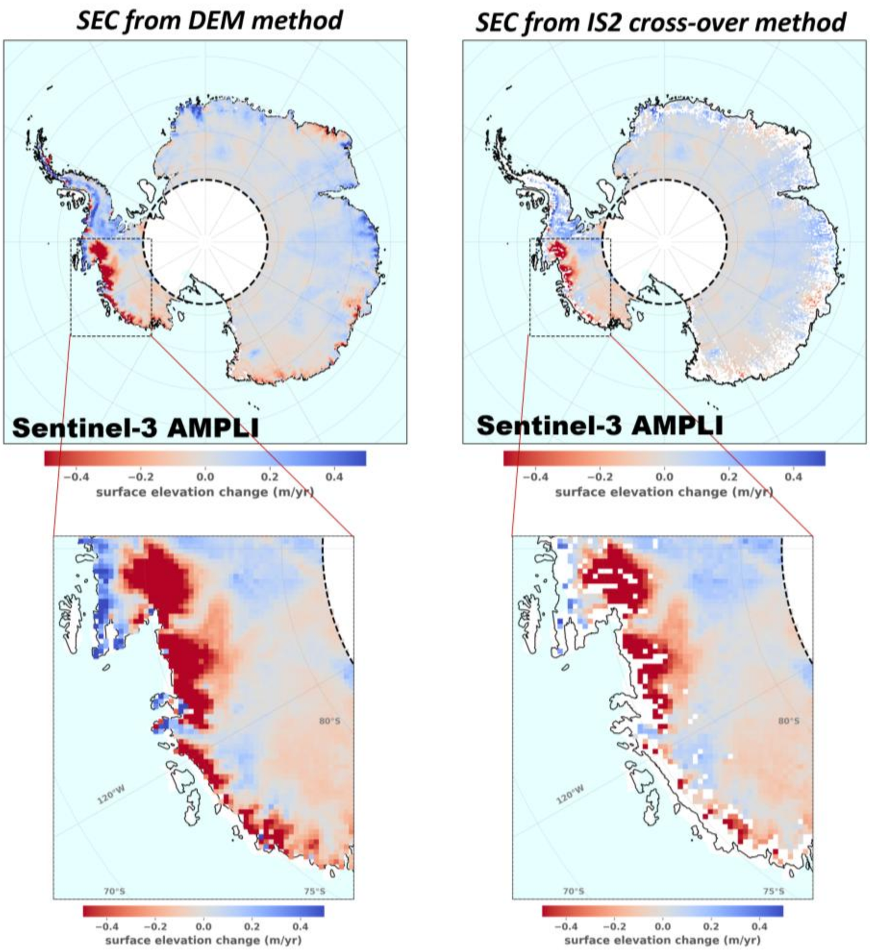

Figure S4: (a) Surface Elevation Change (SEC) of the Antarctic ice sheet over the 2019-2022 period. The SEC is estimated with Sentinel-3A and Sentinel-3B measurements processed by AMPLI, using the DEM method presented section 4.4 (left) and with an alternative method performed through cross-over to ICESat-2, as presented in this supplementary material (right). Grid resolution is 20 km.

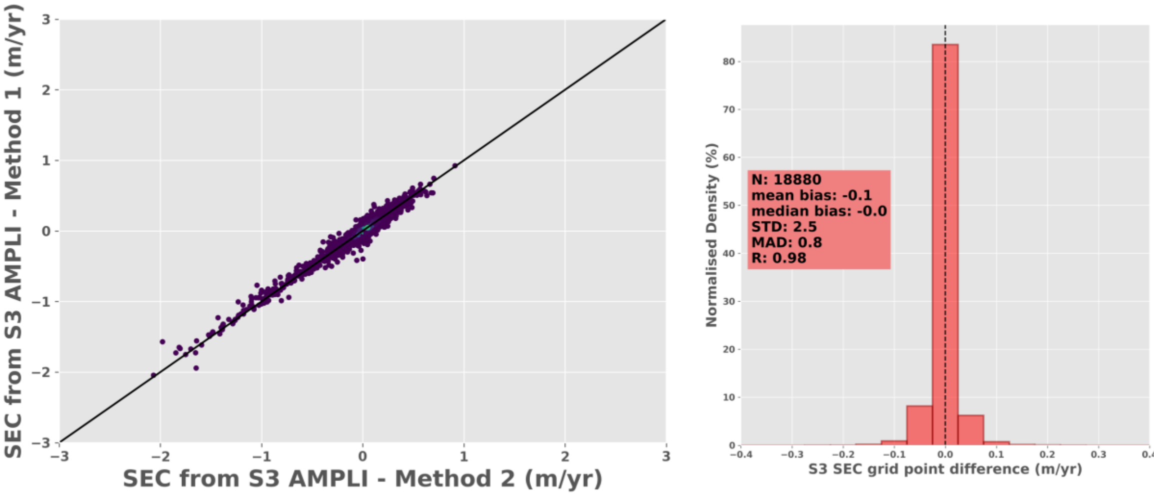

Figure S5: (a) Scatter plot of the SEC grid point differences, as estimated with Sentinel-3 through the DEM method presented section 4.4 (method 1), and with the ICESat-2 cross-over method, as presented above in this supplementary material (method 2). (b) Histogram of the grid point differences.

Section S6: Sentinel-3 AMPLI and ICESat-2 elevation differences in the Antarctic ice sheet interior (section 5.1)

In this section, we complement the investigations made in the East Antarctic Ice Sheet (EAIS) interiors, related to snow volume scattering effect.

The two first figures below (Fig. S6a and Fig. S6b) show the gridded median elevation bias between surface height estimates from Sentinel-3 AMPLI and ICESat-2 ATL06. As described in section 5.1, the analyses are restricted to the East Antarctic Ice Sheet (EAIS) interiors, where surface elevation is above 2,500 meters, surface slope is below 0.2° and SEC is below than 5 cm yr^{-1} in the 2019-2022 period (according to ICESat-2 ATL15 product). Fig. S6a is the same result as presented in section 3, with Sentinel-3 and ICESat-2 measurements acquired in 2019 (except for the geographical selection). Fig. S6b is the equivalent analysis, made with Sentinel-3A and Sentinel-3B measurements acquired in 2022 (data set used for the SEC computation, presented section 4.1). As written in section 5.1, the elevation bias between Sentinel-3 and ICEsat-2 ATL06 depict spatial variations, that are differently distributed in space between 2019 and 2022 analysis.

Fig. S6c shows the difference between maps in Fig. S6b and Fig. S6a (divided by a factor of 3, to convert into meter yr^{-1} unit). Fig. S6d displays the Sentinel-3 SEC estimated with Sentinel-3 in this study over the analysis region (extracted from the global map shown in Fig. 7). The two maps, Fig. S6c and Fig. S6d, are in high correlation, with a ~0.95 Pearson Correlation Coefficient between the map grid points. Because the surface topography is assumed stable in this area (below 5 cm yr^{-1}), this most likely indicates that the SEC estimated by Sentinel-3 over this region is artificially driven by the snow volume scattering. This result emphasizes the need for a snow volume scattering correction, as discussed in section 6.2.

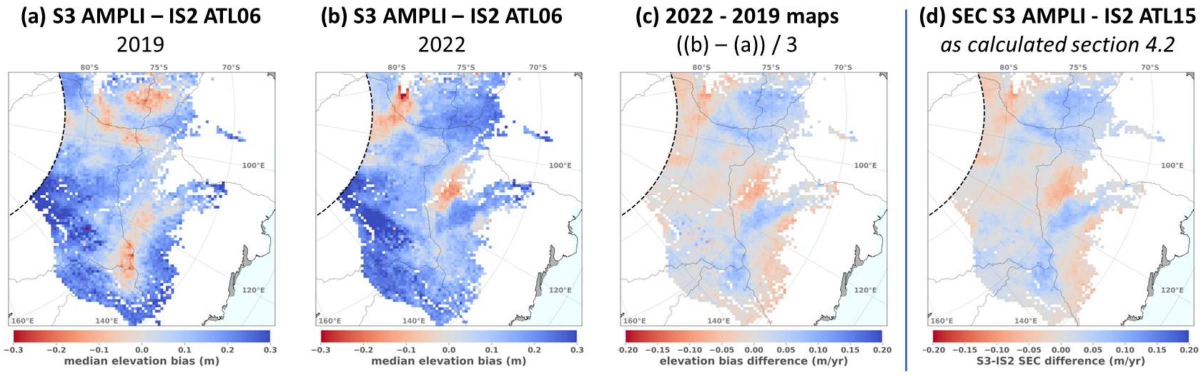

Figure S6: (a) Gridded statistics of the median elevation bias between Sentinel-3 and ICESat-2 ATL06 co-located elevations, for measurements acquired in the 2019 Antarctic winter (b) Same map with Sentinel-3 and ICESat-2 measurements acquired in the 2022 Antarctic winter (c) Difference between the two first maps, divided by a factor of 3 to convert in m yr-1 unit (d) 2019-2022 SEC of the Antarctic ice sheet calculated in the frame of this study with Sentinel-3 AMPLI. The analysis is performed over the ice sheet interior (surface elevation above 2,500 meters, surface slope below 0.2° and ICESat-2 ATL15 SEC below 5 cm yr-1). Grid resolution is 20 km.

Section S7: Illustration of AMPLI simulation over the Antarctic ice sheet interior (section 5.3)

Fig. S7 is a figure equivalent to Fig. 1 (in the main text), but for a Sentinel-3A measurement acquired in the East Antarctic ice sheet interior. The surface slope is estimated at 0.05°. Fig. S8 below displays the Sentinel-3 and the AMPLI UF-SAR waveforms for this measurement. Waveform shape differences are mainly observed in the trailing edge part. We assume this is because snow volume scattering is not yet included in the modelling.

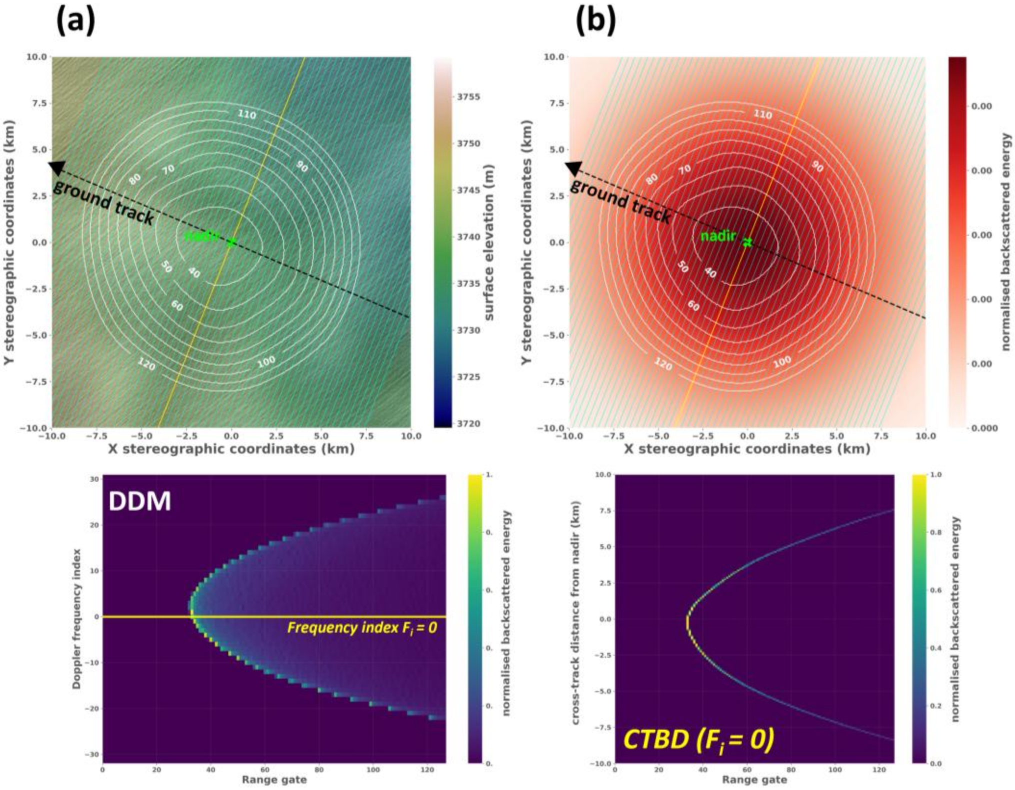

Figure S7: Same plots as Fig. 1 in the publication, but for a Sentinel-3A measurement acquired in the East Antarctic ice sheet. (a) Topography from REMA, over which the simulation is performed (only a 20 km x 20 km area is represented). The white contours display the iso-range lines Ri, the cyan lines represent the 64 delay-Doppler frequencies (b) Energy backscattered at snow-air interface Pfs (c) Delay-Doppler Map simulated by integrating the energy Pfs , given the satellite-facet distance in slant range and in along-track (d) Cross-Track Backscatter Distribution, showing the histogram of the energy Pfs in the cross-track direction, along for the Doppler frequency index n°0.

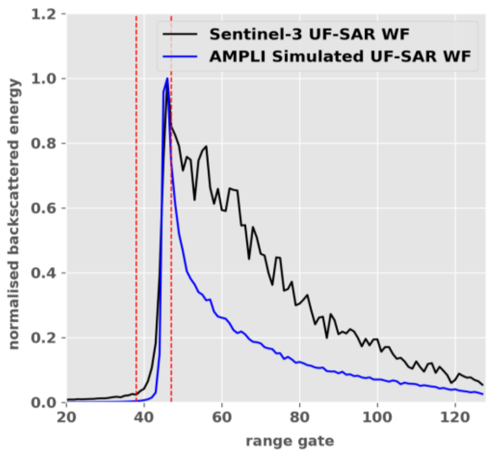

Figure S8: Simulated (blue) and measured (black) Sentinel-3 UF-SAR waveforms for the same measurement as shown in Fig. S7.

Section S8: Impact of a bias in the input DEM used for the facet-based simulation

In this analysis, artificial vertical elevation biases (fixed offset) were introduced in REMA to assess the impact on the surface topography retrieved with the AMPLI software. These bias values are ranging from −5 m to +5 m, in increments of 2.5 m, same intervals as taken by Huang et al. (2024, section 4.5). The processing chain was run with these configurations over the orbit cycle n°45 of Sentinel-3A (acquisitions from 17 May to 13 June, 2019). As reference data set, the AMPLI software was also run in its "nominal" configuration (i.e. no bias in the input DEM). The surface elevation from Sentinel-3A and ICESat-2 ATL06 is compared at nearly co-located points, following the methodology described in section 3. The spatial search radius was enlarged, from 25 m to 50 m, to increase the population of co-located points.

Table S4 displays the median bias and Median Absolute Deviation (MAD) between Sentinel-3A and ICESat-2 ATL06 for several slope ranges (same ones as in Table 1). The median bias between Sentinel-3A and ICESat-2 ATL06 was found to be identical in the few centimetres range, between the five configurations tested, and for all slope bins. The population of co-located measurements slightly decreases over the ice sheet margins when the vertical bias added to the DEM increases, as more measurements are rejected when controlling the vertical bias between DEM and altimetry data. In fact, when checking the agreement between the simulated and the measured waveform, the absolute range bias between both must remain below 30 gates (~14 m), as stated in supplementary section S3.

In Fig. S9, the elevation bias between Sentinel-3A and ICESat-2 ATL06 is mapped using a 100 km stereographic grid (EPSG:3031), for the "nominal" configuration (Fig. S9a) and those with +5 m (Fig. S9b) and -5 m (Fig. S9c) elevation biases added in REMA. The differences between the map grid points are plotted in Fig. S9d ("*+5m*" - "*nominal*") and Fig. S9e ("*-5m*" - "*nominal*"). In these maps no major change in performance is detected between the three configurations. The absolute differences between the configurations remain below 5 cm for 92% and 86% of the map grid points, in Fig. S9d and Fig. S9e, respectively. Whereas the effect of a bias in the input DEM can generate several metres of elevation errors with LEPTA and MPI algorithms, as reported in Huang et al. (2024, section 4.5).

This result is crucial, attesting that AMPLI can monitor the vast majority of the polar ice sheets over a period of several years, without noticeable errors introduced in case of temporal elevation changes (if homogeneous over the radar footprint), as discussed section 5.2. This outcome is also corroborated by the high agreement in the SEC estimated by Sentinel-3 AMPLI and ICESat-2 ATL15, as presented in section 4.

Surface Slope		< 0.1°	0.1° - 0.5°	0.5° - 1°	> 1°
Population ($x10^3$ count)	-5 m	94 $x10^3$	133 $x10^3$	16 $x10^3$	3.9 $x10^3$
	-2.5 m	94 $x10^3$	133 $x10^3$	16 $x10^3$	3.8 $x10^3$
	Nominal	94 $x10^3$	133 $x10^3$	15 $x10^3$	3.7 $x10^3$
	+2.5 m	94 $x10^3$	133 $x10^3$	15 $x10^3$	3.5 $x10^3$
	+5m	94 $x10^3$	131 $x10^3$	14 $x10^3$	3.3 $x10^3$
Median bias (m)	-5 m	+0.11	+0.16	+0.35	+0.46
	-2.5 m	+0.11	+0.16	+0.34	+0.45
	Nominal	+0.10	+0.14	+0.31	+0.42
	+2.5 m	+0.11	+0.15	+0.32	+0.45
	+5m	+0.11	+0.14	+0.32	+0.45
MAD (m)	-5 m	0.10	0.16	0.34	0.49
	-2.5 m	0.10	0.16	0.34	0.50
	Nominal	0.10	0.15	0.33	0.50
	+2.5 m	0.10	0.16	0.33	0.50
	+5m	0.10	0.16	0.33	0.49

Table S4: Statistics of the elevation difference between Sentinel-3 AMPLI and ICESat-2 ATL06 nearly co-located measurements (calculated as Sentinel-3 – ICESat-2) over the Antarctic ice sheet, for different slope intervals. Five AMPLI configurations are assessed: the one presented in section 2 ("Nominal") using an unbiased DEM, and four others with vertical biases introduced in REMA, ranging from -5 m to 5 m. The measurements acquired further south than 80°S are not considered in this analysis, in order to mitigate statistical over-representation of southern observations, where the population of co-located measurements significantly increases.

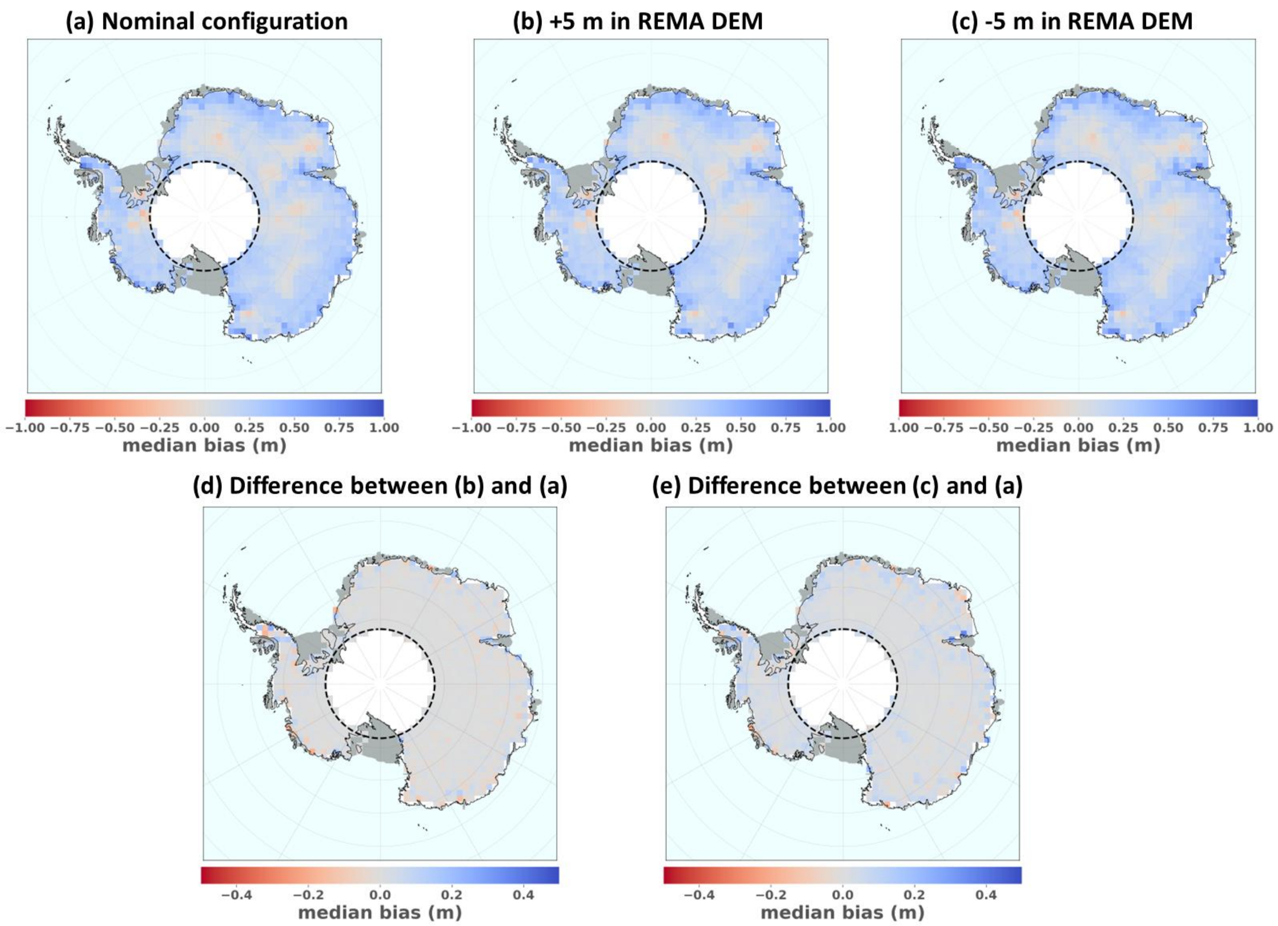

Figure S9: (top panels) Median elevation bias between Sentinel-3 AMPLI and ICESat-2 ATL06 co-located elevations, mapped using a 100 km grid (a) nominal AMPLI configuration, as presented section 2 (b) AMPLI configuration with a +5 m bias introduced in REMA (c) AMPLI configuration with a -5 m bias introduced in REMA. (bottom panels) Map differences between the nominal configuration and ones with +5 m (d) and -5 m (e) biases introduced in REMA.